

# On the Capabilities of Transition Metal Carbides for Carbon Capture and Utilization Technologies

Hector Prats,<sup>\*,†</sup> Arturo Pajares,<sup>‡</sup> Francesc Viñes, Pilar Ramírez de la Piscina, Ramon Sayós, Narcís Homs,<sup>\*</sup> and Francesc Illas



Cite This: *ACS Appl. Mater. Interfaces* 2024, 16, 28505–28516



Read Online

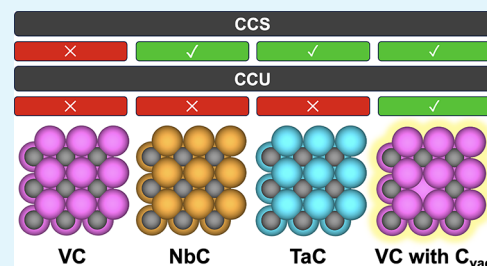
ACCESS |

Metrics & More

Article Recommendations

Supporting Information

**ABSTRACT:** The search for cheap and active materials for the capture and activation of CO<sub>2</sub> has led to many efforts aimed at developing new catalysts. In this context, earth-abundant transition metal carbides (TMCs) have emerged as promising candidates, garnering increased attention in recent decades due to their exceptional refractory properties and resistance to sintering, coking, and sulfur poisoning. In this work, we assess the use of Group 5 TMCs (VC, NbC, and TaC) as potential materials for carbon capture and sequestration/utilization technologies by combining experimental characterization techniques, first-principles-based multiscale modeling, vibrational analysis, and catalytic experiments. Our findings reveal that the stoichiometric phase of VC exhibits weak interactions with CO<sub>2</sub>, displaying an inability to adsorb or dissociate it. However, VC often exhibits the presence of surface carbon vacancies, leading to significant activation of CO<sub>2</sub> at room temperature and facilitating its catalytic hydrogenation. In contrast, stoichiometric NbC and TaC phases exhibit stronger interactions with CO<sub>2</sub>, capable of adsorbing and even breaking of CO<sub>2</sub> at low temperatures, particularly notable in the case of TaC. Nevertheless, NbC and TaC demonstrate poor catalytic performance for CO<sub>2</sub> hydrogenation. This work suggests Group 5 TMCs as potential materials for CO<sub>2</sub> abatement, emphasizes the importance of surface vacancies in enhancing catalytic activity and adsorption capability, and provides a reference for using the infrared spectra as a unique identifier to detect oxy-carbide phases or surface C vacancies within Group 5 TMCs.



**KEYWORDS:** transition metal carbides, heterogeneous catalysis, CO<sub>2</sub> utilization, infrared spectroscopy, C vacancies

## 1. INTRODUCTION

Nowadays, considerable research endeavors are devoted at developing or improving carbon dioxide (CO<sub>2</sub>) capture and conversion technologies,<sup>1–3</sup> mostly fostered by the urgent need of reducing the concentration of CO<sub>2</sub> in the atmosphere. These processes aim at mitigating the CO<sub>2</sub> greenhouse effect and its concomitant effects on the climate change.<sup>4</sup> Here, turning the CO<sub>2</sub> economy into a waste-to-product economy model also appears as an opportunity. Initial efforts lead to the so-called carbon capture and storage (CCS) technologies, requiring to this end materials capable of adsorbing/absorbing significant amounts of CO<sub>2</sub> at normal conditions of temperature and CO<sub>2</sub> partial pressure ( $p_{\text{CO}_2}$ ).<sup>5,6</sup> The inherent chemical stability of a CO<sub>2</sub> molecule complicates this pursuit, requiring materials capable of inducing the necessary charge transfer from the substrate to the adsorbed CO<sub>2</sub> molecule to transform it into an activated, bent CO<sub>2</sub><sup>δ-</sup> species—a prerequisite for utilizing CO<sub>2</sub> as a chemical feedstock in CO<sub>2</sub> capture and utilization (CCU) technologies.<sup>1–3</sup>

First-principles studies based on density functional theory (DFT) proposed transition metal carbides (TMCs) as an appealing family of materials able to capture and activate CO<sub>2</sub> even at stringent conditions of temperature,  $T$ , and  $p_{\text{CO}_2}$ .<sup>7,8</sup> For

some TMCs, such as ZrC and HfC, these conditions could imply temperatures as high as 200 °C and a gas source with a low CO<sub>2</sub> content, such as atmospheric air, with a current CO<sub>2</sub> average content of 40 Pa.<sup>9</sup> Experimental validation of these theoretical predictions followed, with experiments on TiC, ZrC, and VC samples confirming the CO<sub>2</sub> capture capabilities through a combination of X-ray photoemission spectroscopy (XPS) and DFT binding energy estimates.<sup>10</sup>

Further than that, the CO<sub>2</sub> CCS was envisaged on two-dimensional (2D) TMCs even under more stringent conditions,<sup>11,12</sup> a point also experimentally confirmed by selective chemical resolution of CO<sub>2</sub> over N<sub>2</sub>.<sup>13</sup> Even though the CCS capabilities of TMCs are proven, an open question that still needs to be answered is whether such materials are also adequate for CCU technologies *per se*. This is, are such TMCs able to catalyze the CO<sub>2</sub> conversion? For instance, the CO<sub>2</sub> decomposition into CO + O is considered as a textbook

Received: March 5, 2024

Revised: May 16, 2024

Accepted: May 20, 2024

Published: May 24, 2024



example. Would this require some sort of assistance? Or, on the contrary, would the TMCs usage be restricted only to CCS technologies?

To answer these questions, we evaluate here the CCS and possible CCU capabilities of Group 5 TMCs (VC, NbC, and TaC) by combining experimental tests with multiscale modeling from first principles. As shown below, calorimetric CO<sub>2</sub> adsorption measurements align well with theoretical estimates, while the combined analysis of experimental and simulated infrared (IR) spectra unveils potential surface oxidation, leading to the formation of oxy-carbide phases—a well-documented occurrence in TMCs exposed to molecular oxygen.<sup>14</sup> The impact of surface carbon vacancies on CO<sub>2</sub> adsorption and the TMC catalytic behavior is also explored, a phenomenon encountered in the case of VC.<sup>15</sup> Finally, our investigation delves into the configuration of the TMC adlayer across a diverse range of temperatures and CO<sub>2</sub> partial pressure conditions, employing kinetic modeling simulations that consider the effects of diffusion and lateral interactions. This work provides valuable insights into the distinctive CO<sub>2</sub> interaction mechanisms of Group 5 TMCs, shedding light on their potential applications in CCS and CCU technologies while emphasizing the importance of surface vacancies in enhancing their catalytic activity. Moreover, it provides a practical guide to using the IR spectrum as a fingerprint to detect the presence of oxy-carbide phases or surface carbon vacancies in Group 5 TMCs.

## 2. METHODOLOGY

**2.1. Preparation of Samples.** All Group 5 TMC samples were prepared based on a sol–gel method as previously reported.<sup>15</sup> In short, alcoholic solutions of VO(isopropoxide)<sub>3</sub> (Alfa Aesar, 96%), VOCl<sub>3</sub> (Alfa Aesar, 99%), Nb(OC<sub>2</sub>H<sub>5</sub>)<sub>5</sub> (Alfa Aesar, 99.95%), or TaCl<sub>5</sub> (Alfa Aesar, 99.6%) were prepared under Ar. Ethanol was used for VC and NbC preparation; however, due to low solubility of TaCl<sub>5</sub> in ethanol, methanol was used for TaC preparation. For VC, two samples, VC-Pr and VC-Cla, were prepared by using VO(isopropoxide)<sub>3</sub> and VOCl<sub>3</sub> as vanadium precursors, respectively. For the preparation of these two VC samples, 4,5-dicyanoimidazole (Manchester Organics, 96%) was added to the alcoholic solutions as a carbon source. The solution was then stirred until ethanol evaporated resulting in a gel, and the latter was thermally treated under Ar flow at 1373 K for 5 h. In a prior study,<sup>15</sup> we observed the prevalent presence of the V<sub>8</sub>C<sub>7</sub> phase in the vanadium carbide sample prepared using VO(isopropoxide)<sub>3</sub> (VC-Pr). In contrast, the sample prepared using VOCl<sub>3</sub> (VC-Cla) exhibited a higher presence of the stoichiometric VC phase. Additionally, VC-Cla was heated up until 1623 K, resulting in a new sample named VC-Clb with a higher presence of stoichiometric VC, with the aim to analyze the impact of C vacancies. NbC and TaC samples were prepared following the procedure described above but treated under Ar flow at 1473 K for 5 h. After the thermal treatment, samples were contacted with air without previous passivation. The amount of the metal and C precursors added for the preparation of the different samples can be found in Section S1 of the Supporting Information (SI).

**2.2. Characterization.** Powder X-ray diffraction (XRD) measurements were conducted in the range  $2\theta = 4\text{--}100^\circ$ , with a step size of  $0.017^\circ$  and an acquisition time of 80 s per step. The measurements were performed using a PANalytical X'Pert PRO MPD Alpha1 powder diffractometer, utilizing a Ge(111)

primary monochromator and Cu K $\alpha$ 1 radiation source ( $\lambda = 1.5406 \text{ \AA}$ ). The average crystallite size of the transition metal carbide phases was determined using the Debye–Scherrer equation. The specific surface area ( $S_{\text{BET}}$ ) was assessed by conducting multipoint BET analysis on the N<sub>2</sub> adsorption isotherms. N<sub>2</sub> adsorption–desorption isotherms were measured at 77 K by using a Micromeritics Tristar II 3020 instrument. Additionally, the pore size distribution was determined using the BJH (Barret–Joyner–Halenda) method. Scanning electron microscopy (SEM) images were obtained with a ZEISS Auriga instrument operating at an accelerating voltage of up to 20 keV. Transmission electron microscopy (TEM) images were collected employing a JEOL J2010F microscope operated at an accelerating voltage of up to 200 kV. Raman spectra were acquired using a Jobin-Yvon LabRam HR800 spectrometer coupled with an Olympus BXFM microscope, employing a 532 nm laser and a CCD detector. To minimize laser-induced heating effects during data collection, the laser power was restricted to 0.75 mW.

For the H<sub>2</sub>-temperature-programmed reduction (H<sub>2</sub>-TPR) experiments, a Micromeritics AutoChem II 2920 chemisorption instrument was utilized. The samples underwent pretreatment at 363 K under a He atmosphere before being subjected to H<sub>2</sub>/Ar (12% v/v) flow. The temperature was then increased to 1073 K at a rate of 10 K min<sup>-1</sup>.

The adsorption enthalpy of CO<sub>2</sub> onto the different samples was measured using a Sensys evo TG-DSC instrument from Setaram, equipped with a 3D thermal flow sensor and was coupled online to a ThermoStar GSD320T1 mass spectrometer analyzer. The sample (100 mg) was first dried under Ar flow (50 mL min<sup>-1</sup>) at a heating rate of 10 K min<sup>-1</sup> up to 353 K for 30 min. Subsequently, the sample was heated to 823 K at 10 K min<sup>-1</sup> under H<sub>2</sub>/Ar (10% v/v) for 1 h to remove impurities and/or surface oxy-carbide species and then cooled to 303 K under Ar flow. After that, a mixture of CO<sub>2</sub>/He (10% v/v) was introduced to the sample at 303 K with a flow rate of 10 mL min<sup>-1</sup> until no further changes in mass or heat flow were detected. The exothermic peaks corresponding to the adsorption of CO<sub>2</sub> were integrated to determine the total enthalpy of the adsorption. Additionally, the mean adsorption energy for CO<sub>2</sub> was calculated based on the total amount of CO<sub>2</sub> adsorbed during the experiment.

On the other hand, CO<sub>2</sub>, CO, and CO<sub>2</sub>/H<sub>2</sub> (1/3 mol/mol) adsorption experiments were conducted using *in situ* diffuse reflectance infrared spectroscopy (DRIFTS) with a Bruker VERTEX 70 FTIR spectrometer equipped with an MCT detector. This setup included a Harrick Scientific HVCDP-4 catalytic chamber and was coupled online to a ThermoStar GSD320T1 mass spectrometer analyzer. During the experiment, the spectra were acquired by averaging 256 scans at a spectral resolution of 4 cm<sup>-1</sup>. Approximately 30 mg of sample underwent *in situ* treatment within the DRIFTS cell under He flow (20 mL min<sup>-1</sup>) up to 573 K for 30 min. The gas flow was then switched to H<sub>2</sub> for 1 h before cooling the sample to 308 K under He, with the corresponding background spectrum registered. Afterward, in separate experiments, gas mixtures of CO<sub>2</sub>/He (10% v/v), CO/He (10% v/v), or CO<sub>2</sub> (10% v/v)/H<sub>2</sub> (30% v/v)/He were introduced at 308 K with a flow rate of 20 mL min<sup>-1</sup> and allowed to interact with the sample for 20 min. Then, the gas flow was switched to He, and the final spectra were recorded. In every case, the effluent was continuously analyzed by online mass spectrometry (MS). The

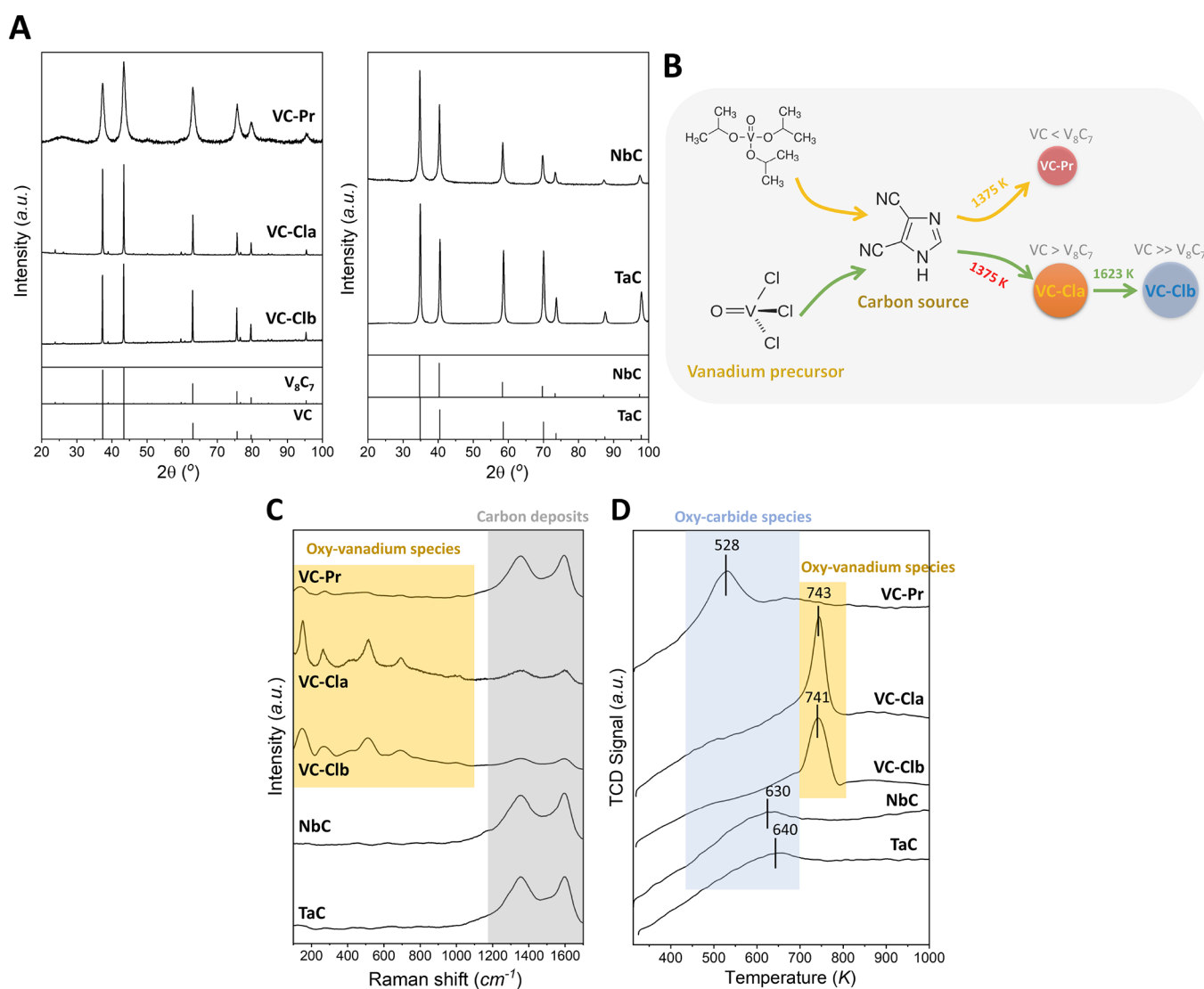


**Figure 1.** Characterization and preparation scheme of as-synthesized Group 5 TMCs: (A) XRD patterns, (B) preparation of the VC samples, (C) Raman spectra, and (D)  $H_2$ -TPR profiles.

$m/z = 30$  signal corresponding to CO was analyzed due to the overlapping of the  $CO_2$  signal at  $m/z = 28$ .

**2.3.  $CO_2$  Reactivity and RWGS Catalytic Test.**  $CO_2$  reactivity and reverse water gas shift (RWGS) reaction studies were performed using a tubular fixed bed reactor made of 316-L stainless steel, measuring 305 mm in length with an inner diameter of 9 mm. A thermocouple was in direct contact with the sample within the reactor setup. Then, 150 mg of sample was diluted within SiC up to 1 mL. For  $CO_2$  reactivity studies, the sample was heated to 873 K under  $N_2$ , and then, a flow of  $CO_2/Ar$  (20%v/v) ( $50 \text{ mL min}^{-1}$ ) was introduced for 140 min.

For the catalytic studies of the RWGS reaction, the sample was initially heated to 573 K under  $N_2$ . Subsequently, a reactant mixture of  $CO_2/H_2/N_2 = 1/3/1$  was introduced into the system with a gas hourly space velocity (GHSV) of  $3000 \text{ h}^{-1}$ . The catalytic behavior of the samples in the RWGS was investigated over a temperature range from 573 to 873 K at a pressure of 1 bar. At each temperature point, the conversion and product distribution were determined by averaging results from at least four separate analyses with each analysis conducted over a period of 2 h at the specified temperature.

The  $CO_2$  conversion ( $X_{CO_2}$ ) and the selectivity toward a specific product  $i$  were defined and calculated as follows:

$$X_{CO_2}(\%) = \left(1 - \frac{(C_{CO_2})_{outlet}}{(C_{CO_2})_{outlet} + \sum (C_i)_{outlet}}\right) \cdot 100 \quad (1)$$

$$S_i(\%) = \frac{(C_i)_{outlet}}{\sum (C_i)_{outlet}} \cdot 100 \quad (2)$$

where  $(C_i)$  and  $C_{CO_2}$  are the molar concentrations of the  $i$  product (CO or  $CH_4$ ), respectively. The analysis and quantification of products for both the  $CO_2$  reactivity and RWGS reaction studies were performed using a Varian 450-GC (Gas Chromatograph) instrument equipped with a thermal conductivity detector (TCD). This instrumentation allowed for accurate measurement and identification of the reaction products.

**2.4. Computational Methods.** DFT calculations were performed using the Vienna *Ab Initio* Simulation Package (VASP) computational suite,<sup>16</sup> using the Perdew–Burke–Ernzerhof (PBE)<sup>17</sup> exchange–correlation ( $xc$ ) functional, and

**Table 1. Crystallite Size (XRD), Amount of Adsorbed CO<sub>2</sub>, CO<sub>2</sub> Adsorption Heat Values at 303 K, and CO Production of Samples at 873 K<sup>d</sup>**

sample	crystallite size (nm)	adsorbed CO <sub>2</sub> (μgCO <sub>2</sub> mg <sub>cat</sub> <sup>-1</sup> )	CO <sub>2</sub> adsorption heat (eV)		CO production
			Exp.	Calc. <sup>a</sup>	(mmolCO kg <sub>cat</sub> <sup>-1</sup> ) <sup>c</sup>
VC-Pr	10	7.40	-0.54	-0.84 <sup>b</sup>	2913
VC-Cla	64	5.94	-0.25	-0.15 <sup>a</sup>	2112
VC-Clb	70	5.52	-0.22	-0.15 <sup>a</sup>	1980
NbC	20	0.89	-1.02	-0.93	271
TaC	22	0.91	-0.94	-1.17	226

<sup>a</sup>VC(001). <sup>b</sup>VC<sub>1-x</sub>(001). <sup>c</sup>From CO<sub>2</sub> reactivity studies. <sup>d</sup>Calculated CO<sub>2</sub> adsorption heats at 303 K have been computed using the ASE thermochemistry module (ref 25).

including dispersion through the D3 method developed by Grimme to account for dispersion interactions.<sup>18</sup> The effect of the core electrons on the valence electron density was described by the Projected Augmented Wave (PAW) method of Blöchl<sup>19</sup> and later implemented in VASP by Kresse and Joubert,<sup>20</sup> whereas the valence electron density was expanded in a plane wave basis set with a cutoff kinetic energy of 520 and 415 eV for bulk and surface calculations, respectively. For bulk structure relaxation, electronic and force convergence tolerances of 10<sup>-6</sup> eV and 10<sup>-3</sup> eV·Å<sup>-1</sup>, respectively, were imposed, and a dense  $\Gamma$ -centered  $k$ -point grid of 80/ $a$  × 80/ $b$  × 80/ $c$  was used, where  $a$ ,  $b$ , and  $c$  are the lattice vectors. The slab models for the stoichiometric carbides (i.e., TMCs, TM = V, Nb, or Ta) were constructed from the optimized bulk structures. The slab models for the corresponding carbides with a surface C vacancy (i.e., TMC<sub>1-x</sub>) were constructed by removing a surface C atom from the TMC slab models and reoptimizing. Finally, the slab models for the corresponding oxycarbides (i.e., TMOc) were constructed by replacing all surface C atoms by O atoms.

To avoid interactions between the periodically repeated slab images, a vacuum width of at least 18 Å was added between the interleaved slabs and a dipole correction was applied along the vacuum direction. For the structure optimization of the clean slab models, the adsorbed species, and the calculation of the transition states (TS), electronic and force convergence tolerances of 10<sup>-5</sup> eV and 10<sup>-2</sup> eV·Å<sup>-1</sup>, respectively, were imposed, and a  $\Gamma$ -centered  $k$ -point grid of 60/ $a$  × 60/ $b$  × 1 was used. Note that when calculating the number of  $k$ -points in a specific direction, noninteger values were rounded up to the nearest integer. The formation energy of CO<sub>2</sub>, CO, and O species ( $E_{fi}$ ) is calculated with respect to gas-phase CO<sub>2</sub> and O<sub>2</sub> molecules (see Section S3 in the Supporting Information). The simulated IR spectra were acquired from vibrational analysis, where the intensities are obtained as the square of the change of the dipole moment perpendicular to the surface associated by the vibrational frequency; details from this procedure are found elsewhere.<sup>10,21,22</sup> The CatLearn's Bayesian transition state search module (ML-NEB)<sup>23</sup> was used to locate all the TS, and the vibrational frequencies of the TS were analyzed to check that only one imaginary mode is present. For crystal structure manipulations and data analysis, we used the Python Materials Genomics (pymatgen)<sup>24</sup> and the Atomic Simulation Environment (ASE)<sup>25</sup> Python libraries. The enthalpies and free energies for each species were computed using the ASE thermochemistry module<sup>25</sup> using the ideal gas model for gas-phase molecules and the harmonic oscillator model for adsorbed species.

Kinetic simulations were carried out using the graph-theoretical kinetic Monte Carlo (kMC) approach<sup>26</sup> combined

with cluster expansion Hamiltonians<sup>27,28</sup> for the surface energetics, as implemented in the ZACROS code.<sup>26</sup> The kMC lattice model consists of a 10 × 10 periodic custom grid of two points—or a total of 200 points—representing surface sites, where the different species can adsorb, desorb, react, or diffuse. Two site types were used, namely, tM and tC, to describe top metal (i.e., V, Nb, or Ta) and top carbon sites. The reaction network involves a total set of four reversible reactions, namely, CO<sub>2</sub> and O<sub>2</sub> adsorption, CO<sub>2</sub> dissociation, and O species diffusion (see Table S1 in the Supporting Information). The cluster expansion used in our model includes first-nearest-neighbors pairwise lateral interactions between all possible pairs among CO<sub>2</sub>, CO, and O (see Table S2 in the Supporting Information). The effect of lateral interactions in the energy barriers is modeled by using the Brønsted–Evans–Polanyi (BEP) relations.<sup>28</sup> The kMC input files were automatically generated using the ZacrosTools Python library.<sup>29</sup>

### 3. RESULTS AND DISCUSSION

**3.1. Characterization of As-Synthesized Carbides.** The XRD patterns of all five carbide samples are depicted in Figure 1A. For VC, characteristic peaks at  $2\theta = 37.4, 43.4, 63.0, 75.6,$  and  $79.7^\circ$ , corresponding to cubic V<sub>8</sub>C<sub>7</sub> (JCPDS 35-0786) and/or VC (JCPDS 01-073-0476) phases are observed. Note that in the case of vanadium carbides, the substoichiometric V<sub>8</sub>C<sub>7</sub> phase (1 C vacancy per 8 V atoms) is more stable than the stoichiometric VC phase.<sup>30</sup> In a previous study, we investigated the presence of both stoichiometry VC and V<sub>8</sub>C<sub>7</sub> phases in vanadium carbide samples according to the preparation method employed in this work (cf. Figure 1B).<sup>15</sup> From PED-ASTAR analysis, we determined a prevalent presence of the stoichiometric VC phase in VC-Cla. On the other hand, for VC-Pr, a more accurate fitting indexation was achieved by assuming the presence of the V<sub>8</sub>C<sub>7</sub> phase in most of the analyzed regions.<sup>15</sup> Additionally, VC-Clb was obtained by heating VC-Cla to 1623 K. In this case, it can be assumed that a significant presence of VC phase exists in VC-Clb as the phase transition from V<sub>8</sub>C<sub>7</sub> → VC is favored with an increase in temperature (cf. Figure 1B).<sup>31</sup> Therefore, while all three VC samples contain C vacancies, the concentration of vacancies decreases in the following order: VC-Pr > VC-Cla > VC-Clb. For the NbC sample, the peaks at  $2\theta = 34.7, 40.3, 57.3, 69.7,$   $73.3, 87.1,$  and  $97.4^\circ$  are attributed to the cubic NbC phase (JCPDS 38-1364). Finally, for the TaC sample, peaks at  $2\theta = 34.9, 40.5, 58.5, 70.0, 73.6, 87.5,$  and  $97.9^\circ$  are assigned to the presence of the cubic TaC phase (JCPDS 35-0801). The perfect match of the experimental diffraction patterns with those of standard references, and the absence of additional peaks, points that the concentration of C vacancies in NbC and

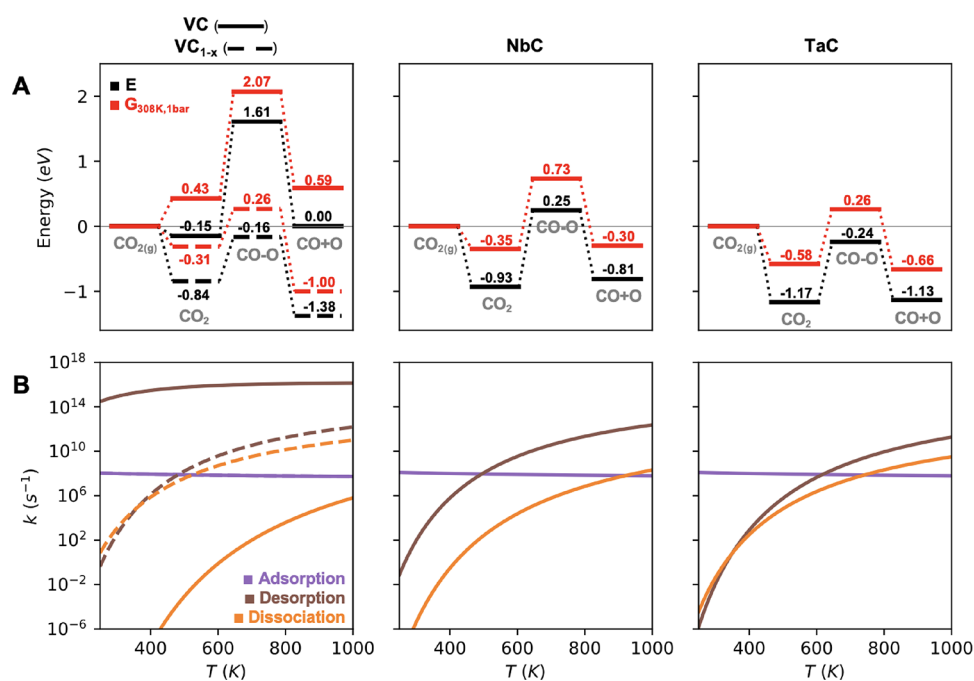


**Figure 2.** (A) Potential energy (black) and Gibbs free energy (red,  $T = 308$  K,  $p_{\text{CO}_2} = 1$  bar) profiles for CO<sub>2</sub> adsorption and dissociation on the (001) surfaces of VC and VC<sub>1-x</sub> NbC, and TaC. The final states correspond to CO and O species at infinite separation (no lateral interaction). Gibbs free energies for gas-phase and adsorbed species have been computed by means of the ideal gas and harmonic oscillator models, respectively, as implemented in the ASE thermochemistry module (ref 25). (B) Rate constants in the temperature range 300–1000 K for CO<sub>2</sub> adsorption (purple,  $p_{\text{CO}_2} = 1$  bar), desorption (brown), and dissociation (orange) on the (001) surfaces of VC, NbC, and TaC. Rate constants have been computed from the partition functions as detailed in the Supporting Information of ref 26.

TaC samples is significantly lower than in the case of the VC samples. This agrees with the DFT-calculated vacancy formation energies, which predict surface C vacancies to be more stable in VC(001) than on either NbC(001) or TaC(001), as shown in Table S3 in the Supporting Information. On the other hand, no XRD peaks indicative of crystalline oxides were detected in any case.

Table 1 presents the crystallite sizes of the samples determined through the XRD analysis. The method used for vanadium carbide preparation influenced the resulting crystallite sizes. VC-Pr, prepared using VO(isopropoxide)<sub>3</sub> as a vanadium precursor, exhibited the smallest crystallite size (10 nm). In contrast, VC-Cla, prepared by using VOCl<sub>3</sub>, showed a larger crystallite size of 64 nm. Heating VC-Cla to 1623 K (VC-Clb) resulted in a slight increase in the vanadium carbide crystallite size, consistent with the findings from TEM analysis (Figure S1). Both NbC and TaC samples demonstrated similar crystallite sizes of approximately 20 and 22 nm, respectively (Table 1).

All samples showed a rather uniform distribution of regular particles with no preferential morphology, as observed from SEM analysis (Figure S2). VC-Pr (315 m<sup>2</sup>g<sup>-1</sup>), VC-Cla (204 m<sup>2</sup>g<sup>-1</sup>), NbC (45 m<sup>2</sup>g<sup>-1</sup>), and TaC (51 m<sup>2</sup>g<sup>-1</sup>) are mesoporous materials, with an average pore size of 3.4–5.1 nm (Figure S3). All samples exhibited Raman bands with peaks centered at 1358 and 1595 cm<sup>-1</sup> (Figure 1C), which are attributed to the presence of residual amorphous carbon resulting from the preparation process. Furthermore, for VC-Cla and VC-Clb, multiple bands were observed within the 100–1100 cm<sup>-1</sup> range. These bands are associated with surface oxy-vanadium species, likely formed during exposure of the samples to air.<sup>32,33</sup> The presence of a low intensity band at 991

cm<sup>-1</sup> may suggest the existence of a very low amount of crystalline V<sub>2</sub>O<sub>5</sub> in both cases.<sup>34</sup> In contrast, VC-Pr displayed significantly lower intense Raman bands in the 100–1100 cm<sup>-1</sup> range compared with VC-Cla and VC-Clb. This suggests a lower presence of surface oxy-vanadium species. NbC and TaC did not show Raman peaks corresponding to NbO<sub>x</sub> and TaO<sub>x</sub>, respectively.<sup>35,36</sup>

H<sub>2</sub>-TPR experiments were conducted on all samples to confirm the presence of oxide species (cf. Figure 1D). In all cases, only very low amounts of hydrogen consumption were determined. The H<sub>2</sub>-TPR profiles of VC-Cla and VC-Clb revealed a H<sub>2</sub> consumption peak at about 743 K of 0.77 and 0.70 mmol H<sub>2</sub> g<sub>cat</sub><sup>-1</sup>, respectively, attributed to the reduction of mono- or polymeric oxy-vanadium species. This is because the reduction of amorphous V<sub>2</sub>O<sub>5</sub> takes place at about 852 K and that of crystalline V<sub>2</sub>O<sub>5</sub> at higher temperatures.<sup>34,37</sup> The minimal H<sub>2</sub> consumption peaks observed for VC-Pr (0.41 mmol H<sub>2</sub> g<sub>cat</sub><sup>-1</sup>), NbC (0.16 mmol H<sub>2</sub> g<sub>cat</sub><sup>-1</sup>), and TaC (0.05 mmol H<sub>2</sub> g<sub>cat</sub><sup>-1</sup>), at temperature ranging from 528 to 640 K, can be associated with the reduction of oxy-carbide species, similar to what has been proposed for MoC<sub>x</sub> catalysts.<sup>38</sup> The more pronounced H<sub>2</sub> consumption peak observed for VC-Cla and VC-Clb in comparison to VC-Pr correlates with the larger presence of oxy-vanadium species in VC-Cla and VC-Clb, as deduced from Raman spectroscopy analysis (cf. Figure 1C). Reductions of Nb<sub>2</sub>O<sub>5</sub> and Ta<sub>2</sub>O<sub>5</sub> are not observed within this temperature range as they take place at higher temperatures (>1173 K).<sup>39</sup>

### 3.2. Strength and Capability of CO<sub>2</sub> Adsorption.

Computed  $E_{\text{ads}}$  values for CO<sub>2</sub> adsorption on the different TMCs show that, while CO<sub>2</sub> interacts weakly with VC (−0.15 eV), the interaction with NbC and TaC is quite strong (−0.93

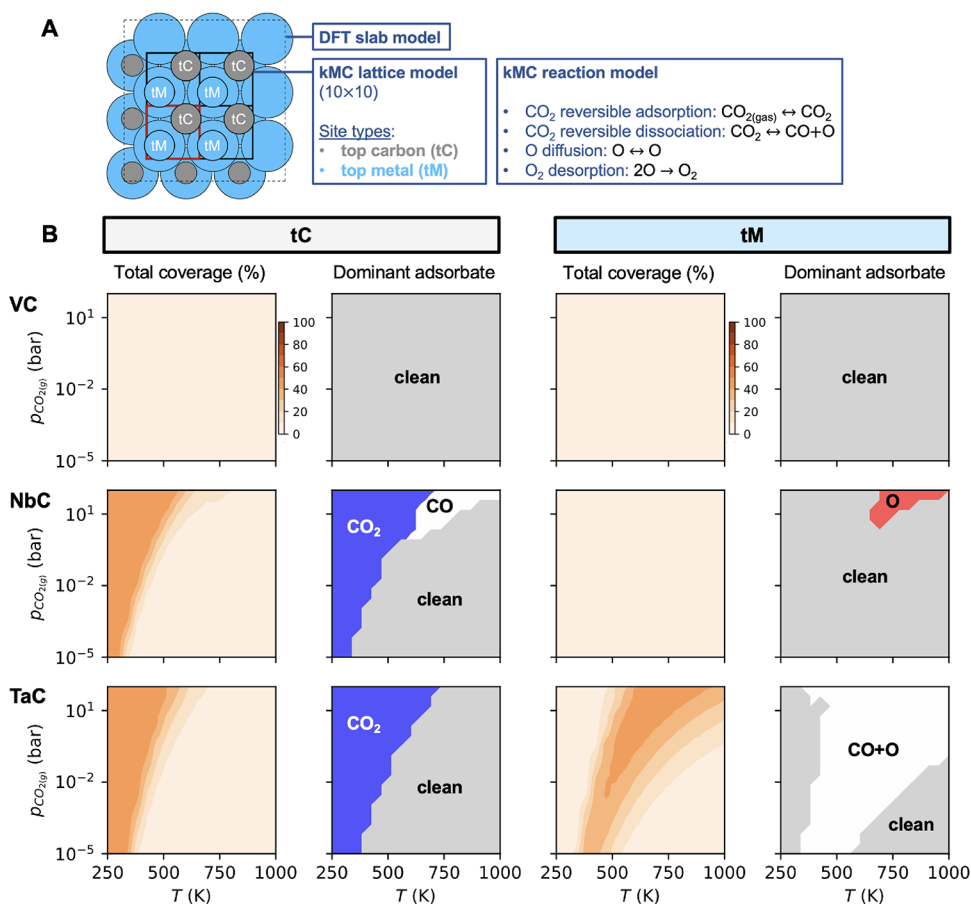


**Figure 3.** (A) Illustration of the DFT slab model and the kMC lattice model (superimposed) and list of the reactions included in the kMC reaction model. Blue and gray spheres represent metal and carbon atoms, respectively. (B) Total coverage and phase diagrams obtained from the kMC simulations as a function of  $\text{CO}_2$  partial pressure ( $10^{-5}$ – $10^2$  bar) and temperature (250–1000 K) for the (001) surfaces of VC, NbC, and TaC. In the phase diagrams, the most dominant species are only shown if the total coverage is higher than 5%. A total of  $3 \times 10^7$  and  $7 \times 10^7$  kMC steps are performed for equilibration and production, respectively, in all kMC simulations.

and  $-1.17$  eV, respectively), as shown in Table 1. Thus,  $\text{CO}_2$  adsorption strength follows the trend  $\text{VC} < \text{NbC} \approx \text{TaC}$ . However, VC can bind  $\text{CO}_2$  almost as strongly as NbC and TaC if C vacancies are present ( $E_{\text{ads}}$  on  $\text{VC}_{1-x}$  is  $-0.84$  eV). The mechanism by which C vacancies enhance the  $\text{CO}_2$  adsorption is explained as follows. Unlike transition metals (TMs), the interaction between TMCs and reaction intermediates is highly influenced by electrostatic interactions. As described in a recent work,<sup>40</sup> the preferred adsorption site does not follow simple valency rules (as opposed to TMs) but correlates with the atomic charge of surface atoms. This is because of the ionic nature of TMCs, where C atoms carry a negative charge and metal atoms carry a positive charge. In a C vacancy site, the surrounding metal atoms are more prone to interact with negatively charged atoms, such as the O atom from  $\text{CO}_2$ . This creates a new adsorption mode for  $\text{CO}_2$  on the vacancy site where one of the two O atoms is directly linked to two neighboring metal atoms (Figure S6), which results in a stronger adsorption compared to the clean carbide.

The measured  $\text{CO}_2$  adsorption heats at 303 K for the different samples agree quite well with the computed DFT values (Table 1). Table 1 also shows the amount of adsorbed  $\text{CO}_2$ . The highest amount of adsorbed  $\text{CO}_2$  and the strongest  $\text{CO}_2$  adsorption heat for the VC-Pr sample can be ascribed to a higher concentration of C vacancies compared to those of VC-Cla and VC-Clb. Moreover, the lower  $\text{CO}_2$  adsorption heat of

VC-Clb compared with VC-Cla confirms the higher prevalence of the stoichiometric VC phase in VC-Clb. On the other hand, for NbC and TaC, the lower amount of adsorbed  $\text{CO}_2$  could be related with their lower surface area. Finally, note that the measured adsorption heats cannot be univocally attributed to  $\text{CO}_2$  as the CO and the O species might also be present. However, Figure 2A shows that the relative stability of adsorbed  $\text{CO}_2$  and CO + O species is very similar, meaning that the computed PBE-D3 values would also agree with the experimental results in the case that  $\text{CO}_2$  dissociates into CO + O. Moreover, as will be shown in Section 3.4, the kMC simulations for the three stoichiometric carbides predict that at 303 K, no CO and/or O species are present.

**3.3. Thermodynamics of  $\text{CO}_2$  Activation.** The computed potential energy and Gibbs free energy profiles in Figure 2A reveal that while  $\text{CO}_2$  dissociation on stoichiometric VC is prohibited (i.e., the potential energy barrier is 1.76 eV), it can occur on NbC and TaC, which exhibit energy barriers of 1.18 and 0.93 eV, respectively. The  $\text{CO}_2$  dissociation ability of VC, however, can be drastically improved when C vacancies are present because the new adsorption sites provided by such C vacancies can lower the energy barrier from 1.76 to only 0.68 eV. The computed free energy profiles show that, at 308 K and  $p_{\text{CO}_2} = 1$  bar,  $\text{CO}_2$  dissociation should be quite feasible on  $\text{VC}_{1-x}$  and TaC, both exhibiting a Gibbs free energy barrier of

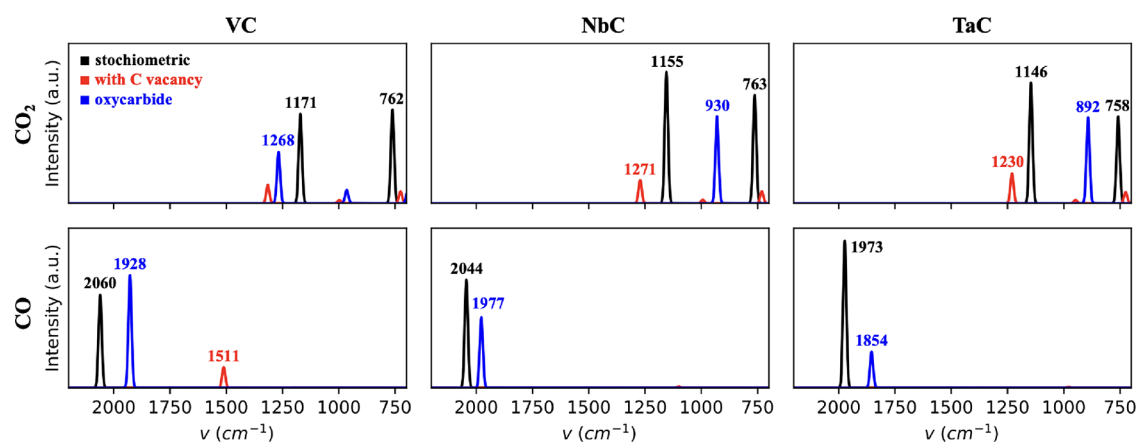


**Figure 4.** Simulated IR spectra in the range 2200–700  $\text{cm}^{-1}$  of either adsorbed  $\text{CO}_2$  (top) and CO (bottom) or VC, NbC, and TaC (left to right). Main peaks are marked with their vibrational frequency. Black, red, and blue peaks correspond to the stoichiometric carbide, the carbide with a surface C vacancy, and the corresponding oxy-carbide.

only 0.26 eV with respect to  $\text{CO}_2(\text{g})$ . For  $\text{VC}_{1-x}$  the dissociated products ( $\text{CO} + \text{O}$ ) are significantly more stable than adsorbed  $\text{CO}_2$ , while in TaC, the dissociation step is almost thermoneutral. For the case of NbC,  $\text{CO}_2$  dissociation is in principle feasible, although at a lower rate since the corresponding Gibbs free energy barrier is 0.73 eV. Finally, the free energy profile for stoichiometric VC suggests that, at these conditions, the surface would be clean as the free energy barrier is 2.07 eV and  $\text{CO}_2$  adsorption would not be favored.

**3.4. Kinetics of  $\text{CO}_2$  activation.** To further evaluate the possible molecular or dissociative chemisorption of  $\text{CO}_2$  on the studied TMCs at a wide range of temperatures, the rate constants for its adsorption, desorption, and dissociation have been estimated from the transition state theory (cf. Figure 2B). For all the temperatures explored, ranging 250–1000 K,  $\text{CO}_2$  desorption is faster than its dissociation on VC and NbC, suggesting that if adsorbed species are present, they will correspond to  $\text{CO}_2$  rather than CO and O. On the contrary,  $\text{VC}_{1-x}$  and TaC feature very similar rate constants for  $\text{CO}_2$  desorption and dissociation, so from the rate constants only, it is not clear what process will dominate. It is worth noting that, for TaC, the rate constant for  $\text{CO}_2$  desorption becomes faster than that of  $\text{CO}_2$  adsorption only above 617 K, which is a significantly higher temperature than that of  $\text{VC}_{1-x}$  (481 K) or NbC (494 K), making TaC a more suitable material for CCS technologies at high temperatures.

To shed some light on the nature of adsorbed species on the TMC surfaces for a wide range of temperatures and partial pressures, we have performed kMC simulations of  $\text{CO}_2$  adsorption and dissociation including the effect of lateral interactions on the stability of adsorbed species and energy barriers as well as diffusion of atomic O species (cf. Figure 3A). The total coverage and the corresponding phase diagrams at 250–1000 K and  $10^{-5}$ – $10^2$  bar for VC, NbC, and TaC are shown in Figure 3B. Note that we have not performed kMC simulations on the  $\text{VC}_{1-x}$  model due to the complexities that arise from a dynamic lattice model in which the number of surface vacancies changes with time. The simulated phase diagrams agree very well with the predictions from the energy profiles and rate constants in Figure 2. For VC, the surface is always empty even at the lowest temperature (250 K) and highest pressure (100 bar) as a result of its very weak interaction with  $\text{CO}_2$ . Therefore, the presence of adsorbed  $\text{CO}_2$  and CO species detected experimentally must be due to

C vacancies. Regarding NbC, the kMC simulations indicate that the surface would be covered by  $\text{CO}_2$  at relatively low temperatures (<300–650 K depending on  $p_{\text{CO}_2}$ ) and clean in the remaining conditions, with the exception of high temperatures and very high pressures (>10 bar) where the most dominant species are CO and O. Finally, in the case of TaC, the kMC simulations indicate the presence of adsorbed  $\text{CO}_2$  species up to 350–700 K (depending on  $p_{\text{CO}_2}$ ) and CO + O at higher temperatures. Only in the case of high temperatures and very low  $p_{\text{CO}_2}$  (< $10^{-2}$  bar), a clean surface can be expected. A similar conclusion is expected for the case of  $\text{VC}_{1-x}$  because the potential energy diagrams are quite alike. Therefore, it is clear that the predicted  $\text{CO}_2$  adsorptive capabilities from the kMC simulations increase in the  $\text{VC} < \text{NbC} < \text{TaC}$  ( $\approx \text{VC}_{1-x}$ ) sequence, even to the point that TaC (and  $\text{VC}_{1-x}$ ) allow the  $\text{CO}_2$  capture and dissociation at near ambient conditions.

**3.5.  $\text{CO}_2$  Reactivity Experiments.** In addition to the calorimetric adsorption studies of  $\text{CO}_2$ , the samples were subjected to  $\text{CO}_2$  flow at 873 K for 140 min and the released CO was quantified (see Table 1 and Figure S4 in the SI). The formation of CO was observed in all cases. VC-Pr exhibited a higher CO production (2913  $\text{mmolCO kg}_{\text{cat}}^{-1}$ ) compared to VC-Cla (2112  $\text{mmolCO kg}_{\text{cat}}^{-1}$ ) and VC-Clb (1980  $\text{mmolCO kg}_{\text{cat}}^{-1}$ ), which is attributed to a higher presence of surface C vacancies on VC-Pr. On the other hand, NbC and TaC produced only 271 and 226  $\text{mmolCO kg}_{\text{cat}}^{-1}$ , respectively. Notably, an initial significant reduction in CO production was observed within the first minutes of reaction in all cases (Figure S4 in the Supporting Information). The XRD patterns obtained after the  $\text{CO}_2$  reactivity experiments at 873 K revealed the formation of crystalline metal oxides in VC-Pr, VC-Cla, VC-Clb, and NbC (Figure S5). No peaks corresponding to crystalline  $\text{TaO}_x$  were detected in TaC. This observation could be attributed to the higher oxidation resistance exhibited by TaC compared to NbC and VC systems.<sup>41,42</sup>

**3.6. Simulated IR spectra.** To interpret the experimental spectra of the three Group 5 TMCs in the presence of  $\text{CO}_2$  and to identify the possible formation of CO or O species, we simulated the IR spectra of  $\text{CO}_2$  and CO species adsorbed on the three TMCs, as shown in Figure 4 and Table 2. According to the simulated spectra, molecular  $\text{CO}_2$  is characterized by the presence of two peaks at  $\sim 760 \text{ cm}^{-1}$  and  $1146\text{--}1171 \text{ cm}^{-1}$ .

**Table 2.** Calculated IR Vibrational Modes (in  $\text{cm}^{-1}$ ) in the Range 2200–700  $\text{cm}^{-1}$  for Adsorbed  $\text{CO}_2$  and CO Species on All TMC Surfaces Considered

surface	$\text{CO}_2$	CO
VC	762: bending 1171: symmetric stretching	2060: stretching
$\text{VC}_{1-x}$		1511: stretching
VOC	1268: asymmetric stretching	1928: stretching
NbC	763: bending 1155: symmetric stretching	2044: stretching
$\text{NbC}_{1-x}$	1271: asymmetric stretching	
NbOC	930: symmetric stretching	1977: stretching
TaC	758: bending 1146: symmetric stretching	1973: stretching
$\text{TaC}_{1-x}$	1230: asymmetric stretching	
TaOC	892: symmetric stretching	1854: stretching

The crucial factor here is that, upon dissociation, the resulting moieties would essentially lead to highly intense signals at 2044–2060  $\text{cm}^{-1}$  for VC and NbC and  $\sim 1973 \text{ cm}^{-1}$  for TaC, which would correspond to the stretching vibration of a perpendicularly adsorbed CO molecule. Due to the possible presence of C vacancies and the possible oxidation of the outermost surface layer, we have also simulated the IR spectrum of adsorbed  $\text{CO}_2$  and CO on a surface vacancy site and on the corresponding oxy-carbide. The presence of surface C vacancies or an oxy-carbide phase can be detected from the IR spectra due to the appearance of new peaks at different frequencies (red and blue peaks in Figure 4). Noticeably, when CO is adsorbed on the corresponding oxy-carbide, the

frequency of the C–O stretching peak is about 100  $\text{cm}^{-1}$  lower compared to the stoichiometric TMC. The optimized geometries for all surface species on all TMC,  $\text{TMC}_{1-x}$ , and TMO slab models are displayed in Figures S6–S8 in the Supporting Information.

**3.7. Experimental IR spectra.** **3.7.1. VC Samples.** Figure 5A (black lines) shows the experimental DRIFT spectra for the adsorption of  $\text{CO}_2$  on VC-Pr and VC-Clb samples in the range 2100–1800  $\text{cm}^{-1}$ , where the stretching vibrations associated with coordinated CO are anticipated. VC-Clb was selected instead of VC-Cla due to a higher predominance of the stoichiometric VC phase. The two peaks observed at 2078–2058  $\text{cm}^{-1}$  are in perfect agreement with the C–O stretching vibrations for adsorbed CO on VC predicted by DFT (Table 2). Meanwhile, the band at a lower wavenumber (1978  $\text{cm}^{-1}$ ) can be attributed to the C–O stretching of CO on VOC. This suggests that both VC-Pr and VC-Clb samples expose VC and VOC phases, in agreement with the Raman bands in Figure 1C. Furthermore, the release of CO from the  $\text{CO}_2$ -DRIFT experiments was monitored via MS analysis, as shown in Figure 5B (black lines). Upon contact of  $\text{CO}_2$  with the samples, the presence of CO was detected within the first 200 s, after which it gradually decreased over time in both samples. This phenomenon may be linked to the diminution of active sites responsible for  $\text{CO}_2$  dissociation (i.e., C vacancies), which are continuously converted into VOC. Notably, this decrease in CO production over time aligns well with the observations made when a  $\text{CO}_2$  stream was passed through the TMCs in the reactor (Figure S4).

After approximately 30 min, the  $\text{CO}_2$  flow was switched to He to remove the potential physisorbed species. The resulting

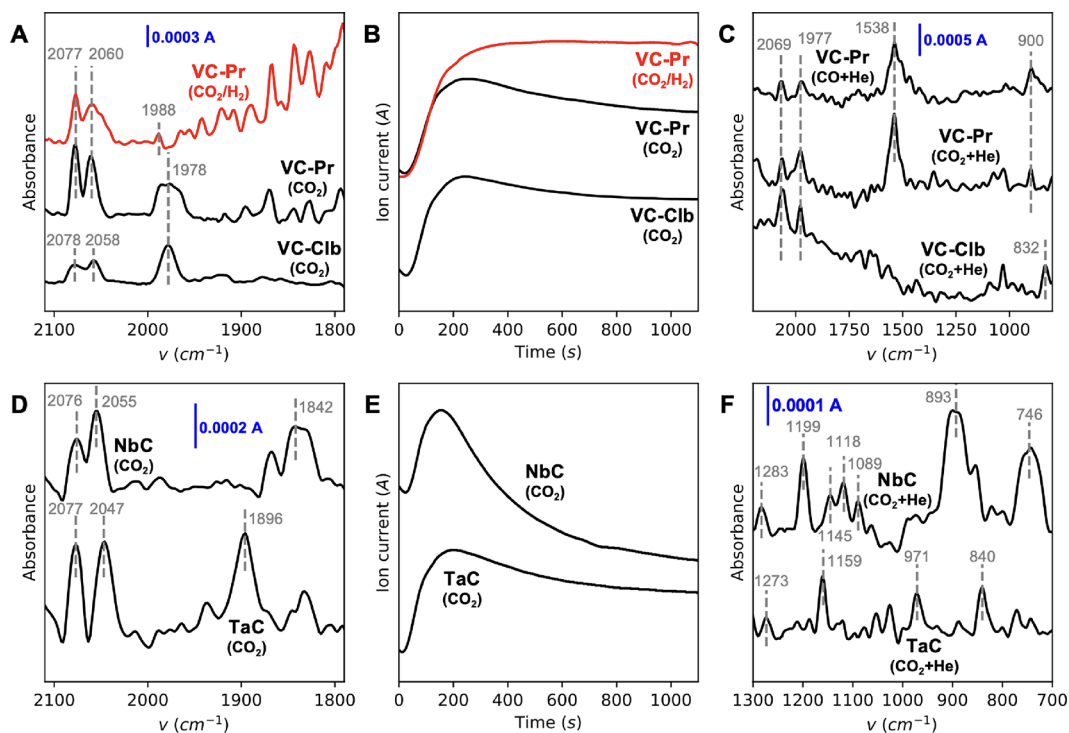


**Figure 5.** (A) Experimental DRIFT spectra after  $\text{CO}_2$  adsorption over VC-Pr and VC-Clb and after  $\text{CO}_2/\text{H}_2$  adsorption over VC-Pr. (B) CO MS profile ( $m/z = 30$ ) after  $\text{CO}_2$  adsorption over VC-Pr and VC-Clb and after  $\text{CO}_2/\text{H}_2$  adsorption over VC-Pr. (C) Experimental DRIFT spectra after the adsorption of  $\text{CO}_2$  and He flushing over VC-Pr and VC-Clb and after CO adsorption and He flushing over VC-Pr. (D) Experimental DRIFT spectra after  $\text{CO}_2$  adsorption over NbC and TaC. (E) CO MS profile ( $m/z = 30$ ) after  $\text{CO}_2$  adsorption over NbC and TaC. (F) Experimental DRIFT spectra after the adsorption of  $\text{CO}_2$  and He flushing over NbC and TaC;  $T = 308 \text{ K}$ .

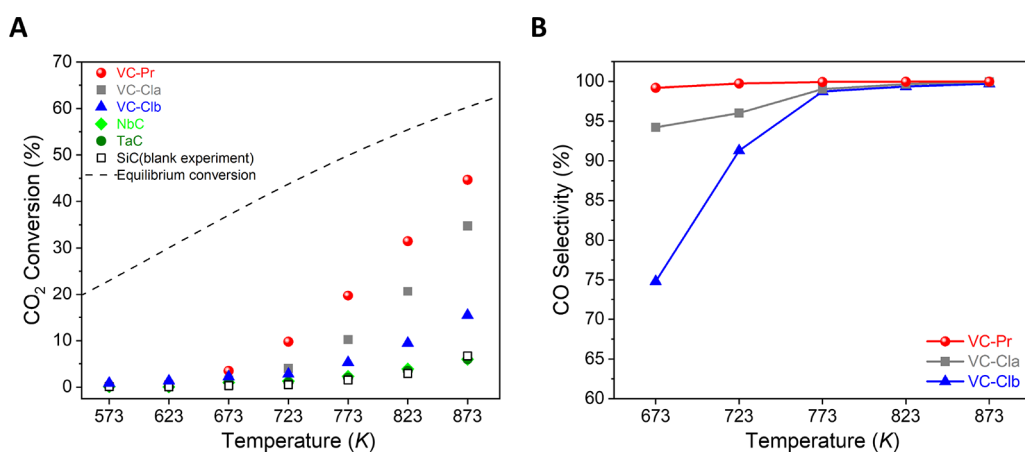


**Figure 6.** Catalytic behavior of the Group 5 TMCs in the RWGS reaction as a function of reaction temperature: (A) CO<sub>2</sub> conversion and (B) CO selectivity. Reaction conditions:  $m_{\text{cat}} = 150$  mg,  $\text{CO}_2/\text{H}_2/\text{N}_2 = 1/3/1$ , GHSV = 3000 h<sup>-1</sup>,  $p = 1$  bar.

DRIFT spectra for VC-Pr and VC-Clb, recorded in the wavenumber range of 2200–800 cm<sup>-1</sup>, are depicted in Figure 5C. The previously mentioned bands, now centered at 2069 and 1977 cm<sup>-1</sup>, remain visible, indicating the presence of chemisorbed CO species. Additionally, a well-defined band at 1538 cm<sup>-1</sup> is observed in the spectrum of VC-Pr but is absent in the spectrum of VC-Clb. According to simulated IR calculations, this band can be attributed to the presence of surface C vacancies (C–O stretching on the VC<sub>1-x</sub> model, see Table 2), in perfect agreement with the higher concentration of C vacancies of VC-Pr compared to VC-Clb. To validate the attribution of the aforementioned IR bands to different coordinated CO species, a separate CO adsorption experiment was conducted for the VC-Pr sample. Following CO adsorption and subsequent He flushing, the *in situ* DRIFT spectrum, presented in Figure 5C, displays bands at 2069, 1977, and 1538 cm<sup>-1</sup>, consistent with those observed previously.

In a separate experiment, the adsorption of a mixture of CO<sub>2</sub>/H<sub>2</sub> = 1/3, simulating conditions of the RWGS reaction, was conducted over the VC-Pr sample. The DRIFT spectrum presented in Figure 5A (red line) exhibits similar yet broader bands in the range of 2077–2060 cm<sup>-1</sup> under the CO<sub>2</sub>/H<sub>2</sub> flow. However, a less intense band at 1988 cm<sup>-1</sup> was observed in this case. As discussed previously, the band at 1988 cm<sup>-1</sup> is likely attributed to the C–O stretching of CO over surface oxy-carbide species (cf. Table 2). The use of the CO<sub>2</sub>/H<sub>2</sub> mixture instead of pure CO<sub>2</sub> flow may facilitate the continuous conversion of VOC species on the surface by removing surface oxygen species with H<sub>2</sub>. Under these conditions, the online MS analysis indicates a continuous production of CO (red line in Figure 5B).

**3.7.2. NbC and TaC samples.** Figure 5D displays the recorded CO<sub>2</sub>-DRIFT spectra for the NbC and TaC samples. Upon CO<sub>2</sub> adsorption on the NbC sample, bands observed in the range of 2076–2055 cm<sup>-1</sup>, along with a broad absorption peak centered at 1842 cm<sup>-1</sup>, can be associated with coordinated CO on stoichiometric NbC and NbOC species, respectively (cf. Table 2). Similarly, for the TaC sample, bands in the range 2077–2047 cm<sup>-1</sup> and a peak at 1896 cm<sup>-1</sup> are indicative of coordinated CO on stoichiometric TaC and TaOC species, respectively (Table 2). The positions of these bands align quite well with those obtained from the simulated IR spectra (Figure 4).

The release of CO from CO<sub>2</sub> adsorption on NbC and TaC samples was also monitored using online MS analysis (cf. Figure 5E). CO was detected within the first 200 s of CO<sub>2</sub> adsorption, after which the evolution of the CO gradually decreased with time on both samples. Furthermore, after approximately 30 min, the flow of CO<sub>2</sub> was switched to He to remove physisorbed species. Figure 5F illustrates the CO<sub>2</sub>-DRIFT spectra of NbC and TaC after He flushing, within the wavenumber range 1300–700 cm<sup>-1</sup>. For NbC, the dominant presence of a stoichiometric NbC phase is indicated by the bands at 746 cm<sup>-1</sup> (CO<sub>2</sub> bending) and in the range 1089–1199 cm<sup>-1</sup> (CO<sub>2</sub> stretching), according to Table 2. The intense band observed at 893 cm<sup>-1</sup> indicates the presence of an oxy-carbide phase (CO<sub>2</sub> stretching on NbOC). The small band at 1283 cm<sup>-1</sup> might indicate the presence of some surface C vacancies. Regarding TaC, the presence of a stoichiometric TaC phase is indicated by the strong band at 1159 cm<sup>-1</sup> (CO<sub>2</sub> stretching). The bands at 840 and 971 cm<sup>-1</sup> could be attributed to the CO<sub>2</sub> stretching on TaOC. Finally, the very small band at 1273 cm<sup>-1</sup> could indicate the presence of some surface C vacancies (CO<sub>2</sub> stretching on TaC<sub>1-x</sub>). Thus, the presence of C vacancies cannot be ruled out in NbC and TaC samples, although its concentration is expected to be much lower compared to that in the VC samples, because the intensities of the bands at 1283 and 1273 cm<sup>-1</sup> for NbC and TaC are at least 10 times lower than that of the band at 1538 cm<sup>-1</sup> for VC-Pr (see Figure 5C,F).

The detection of adsorbed CO<sub>2</sub> in the CO<sub>2</sub>-DRIFT spectra of NbC and TaC following He flushing suggests a stronger adsorption of molecular CO<sub>2</sub> on NbC and TaC compared to that of VC samples. This finding is consistent with the CO<sub>2</sub> adsorption heat values obtained in TGA experiments (refer to Table 1), where NbC and TaC displayed higher CO<sub>2</sub> adsorption heat values compared to those of VC samples. Moreover, DRIFTS results confirmed the coexistence of stoichiometric and oxy-carbide surfaces in both NbC and TaC samples and suggested the possible presence of surface C vacancies, although to a very minor extent compared to the VC samples.

**3.8. RWGS Catalytic Tests.** Based on the above experiments, it becomes apparent that all of the considered samples can capture and activate CO<sub>2</sub> at room temperature. Notably, in the case of VC samples, this ability stems exclusively from the presence of surface carbon vacancies. Consequently, we

investigated the potential use of such carbides as CO<sub>2</sub> hydrogenation catalysts by means of the RWGS reaction. As depicted in Figure 6, only the VC samples among all the tested materials are active toward the RWGS. The observed trend in CO<sub>2</sub> conversion and CO selectivity—VC-Pr > VC-Cla > VC-Clb—is closely tied to the concentration of highly active surface C vacancy sites. Conversely, NbC and TaC exhibit poor catalytic activity. In fact, the poor performance of the stoichiometric Group 5 TMCs was predicted in a previous DFT study,<sup>43</sup> given their very weak interaction with H<sub>2</sub> and the endoergonicity of the H<sub>2</sub> dissociation reaction. However, the presence of surface C vacancies allows for a much stronger binding of H species, i.e., the adsorption energies for adsorbed H species on VC and VC<sub>1-x</sub> are -2.03 and -2.91 eV, respectively,<sup>15</sup> and also facilitates H<sub>2</sub> dissociation, given that the potential energy barriers for H<sub>2</sub> dissociation on VC and VC<sub>1-x</sub> are 0.65 and 0.16 eV, respectively.<sup>15</sup> Therefore, our results validated these theoretical predictions, and the poor RWGS activity of NbC and TaC can be attributed to their feeble interaction with adsorbed H<sub>2</sub> or H species and presumably also to their limited concentration of C vacancies.

#### 4. CONCLUSIONS

The present study evaluates the potential of VC, NbC, and TaC as materials for CCS and CCU technologies. In the case of VC, the C-defective V<sub>8</sub>C<sub>7</sub> phase is more stable than the stoichiometric (cubic) VC phase, and three different samples with varying concentrations of C vacancies are prepared and examined. This is not the case for NbC and TaC, where the stoichiometric phase is predominant. Calorimetric measurements of adsorbed CO<sub>2</sub> align closely with the present PBE-D3 calculations on CO<sub>2</sub> adsorption, validating the computational methodology. Subsequently, free energy diagrams for CO<sub>2</sub> dissociation and kMC simulations are employed to predict the surface composition of VC, NbC, and TaC under different conditions of  $p_{\text{CO}_2}$  and  $T$ , leading to the construction of phase diagrams. This information is compared with experimental DRIFT spectra after CO<sub>2</sub> adsorption. To interpret the experimental IR spectra, we compute the interaction of CO<sub>2</sub>, CO, and O with DFT not only on the stoichiometric TMC models but also on slab models with a surface C vacancy (TMC<sub>1-x</sub>) and their corresponding oxy-carbides (TMOC). Then, we simulate the IR spectra through vibrational analysis and use this information to reveal the presence of C vacancies and the oxy-carbide phase on the different samples.

Our findings reveal that VC is a promising material for CCU owing to the critical role played by surface C vacancies, which are found in abundance in this material. Without these vacancies, VC would weakly interact with CO<sub>2</sub>, much less dissociate it. Conversely, NbC and TaC show potential for CCS due to their strong interaction with CO<sub>2</sub>, and in the case of TaC, it can easily dissociate CO<sub>2</sub> to CO + O at a low temperature. However, both NbC and TaC show poor intrinsic catalytic performance for CO<sub>2</sub> hydrogenation *per se*, and we attribute this result to the much lower concentration of C vacancies present in these carbides. The present catalytic tests have also validated earlier theoretical predictions suggesting that the stoichiometric phases of Group 5 TMCs exhibit poor performance in the hydrogenation of CO<sub>2</sub>.<sup>42</sup> We propose that the catalytic activity for NbC and TaC could also be improved by the incorporation of C vacancies through novel preparation methods, or using promoters, such as small

metal clusters.<sup>8,44</sup> This study advocates for the use of Group 5 TMCs in CCS or CCU technologies, offers a guide on utilizing IR spectra as a fingerprint for identifying oxy-carbide phases or surface C vacancies within Group 5 TMCs, and highlights the importance of surface C vacancies in the adsorptive and catalytic properties of TMCs.

#### ■ ASSOCIATED CONTENT

##### Supporting Information

The Supporting Information is available free of charge at <https://pubs.acs.org/doi/10.1021/acsami.4c03735>.

Additional details on the experimental and theoretical techniques, plots of CO production from CO<sub>2</sub> reactivity studies, XRD patterns of samples after CO<sub>2</sub> reactivity, illustrations of all adsorbed configurations on TMC, TMC<sub>1-x</sub> and TMOC slab models (TM = V, Nb, and Ta), and calculated vacancy formation energies (PDF)

#### ■ AUTHOR INFORMATION

##### Corresponding Authors

**Hector Prats** – Department of Chemistry, Physical and Theoretical Chemistry Laboratory, University of Oxford, Oxford OX1 3QZ, U.K.; [orcid.org/0000-0003-4991-253X](https://orcid.org/0000-0003-4991-253X); Email: [hector.pratsgarcia@chem.ox.ac.uk](mailto:hector.pratsgarcia@chem.ox.ac.uk)

**Narcis Homs** – Departament de Química Inorgànica i Orgànica, Secció de Química Inorgànica and Institut de Nanociència i Nanotecnologia (IN2UB), Universitat de Barcelona, Barcelona 08028, Spain; Institut de Recerca en Energia de Catalunya (IREC), Barcelona 08930, Spain; [orcid.org/0000-0002-0847-7327](https://orcid.org/0000-0002-0847-7327); Email: [narcis.homs@qi.ub.es](mailto:narcis.homs@qi.ub.es)

##### Authors

**Arturo Pajares** – Sustainable Materials, Flemish Institute for Technological Research (VITO NV), Mol 2400, Belgium; [orcid.org/0000-0002-0160-2770](https://orcid.org/0000-0002-0160-2770)

**Francesc Viñes** – Departament de Ciència de Materials i Química Física & Institut de Química Teòrica i Computacional (IQTUB), Universitat de Barcelona, Barcelona 08028, Spain; [orcid.org/0000-0001-9987-8654](https://orcid.org/0000-0001-9987-8654)

**Pilar Ramírez de la Piscina** – Departament de Química Inorgànica i Orgànica, Secció de Química Inorgànica and Institut de Nanociència i Nanotecnologia (IN2UB), Universitat de Barcelona, Barcelona 08028, Spain; [orcid.org/0000-0003-4116-5891](https://orcid.org/0000-0003-4116-5891)

**Ramon Sayós** – Departament de Ciència de Materials i Química Física & Institut de Química Teòrica i Computacional (IQTUB), Universitat de Barcelona, Barcelona 08028, Spain; [orcid.org/0000-0001-6627-7844](https://orcid.org/0000-0001-6627-7844)

**Francesc Illas** – Departament de Ciència de Materials i Química Física & Institut de Química Teòrica i Computacional (IQTUB), Universitat de Barcelona, Barcelona 08028, Spain; [orcid.org/0000-0003-2104-6123](https://orcid.org/0000-0003-2104-6123)

Complete contact information is available at: <https://pubs.acs.org/doi/10.1021/acsami.4c03735>

##### Author Contributions

<sup>¶</sup>H.P. and A.P. contributed equally.

## Notes

The authors declare no competing financial interest.

## ACKNOWLEDGMENTS

The authors thank the Spanish Ministerio de Ciencia e Innovación (MCIN) and Agencia Estatal de Investigación (AEI) MCIN/AEI/10.13039/501100011033 for PID2020-116031RB-I00, PID2020-115293RJ-I00, PID2021-126076NB-I00, PID2022-138180OB-I00, and TED2021-129506B-C22 projects, funded partially by FEDER Una manera de hacer Europa, as well as for the Unidad de Excelencia María de Maeztu CEX2021-001202-M granted to the IQTCUB. COST Action CA18234 is acknowledged. Generalitat de Catalunya funding is also acknowledged through 2021SGR00079 and 2023 CLIMA 00009 AGAUR grants. F.V. thanks the ICREA Academia Award 2023 ref. Ac2216561. A.P. thanks MINECO for the PhD grant BES-C-2015-074574.

## REFERENCES

- (1) Freund, H.; Roberts, M. W. Surface Chemistry of Carbon Dioxide. *Surf. Sci. Rep.* **1996**, *25*, 225–273.
- (2) Burghaus, U. Surface science perspective of carbon dioxide chemistry—Adsorption kinetics and dynamics of CO<sub>2</sub> on selected model surfaces. *Catal. Today* **2009**, *148*, 212–220.
- (3) Taifan, W.; Boily, J.-F.; Baltrusaitis, J. Surface Chemistry of Carbon Dioxide Revisited. *Surf. Sci. Rep.* **2016**, *71*, 595–671.
- (4) Edenhofer, O.; Pichs-Madruga, R.; Sokona, Y.; Minx, J. C.; Farahani, E.; Susanne, K.; Seyboth, K.; Adler, A.; Baum, I.; Brunner, S.; Eickemeier, P.; Kriemann, B.; Savolainen, J.; Schöler, S.; von Stechow, C.; Zwickel, T.; *Climate Change 2014: Mitigation of Climate Change*, 2014.
- (5) Espinal, L.; Poster, D. L.; Wong-Ng, W.; Allen, A. J.; Green, M. L. Measurement, Standards, and Data Needs for CO<sub>2</sub> Capture Materials: A Critical Review. *Environ. Sci. Technol.* **2013**, *47*, 11960–11975.
- (6) D'Alessandro, D. M.; Smit, B.; Long, J. R. Carbon Dioxide Capture: Prospects for New Materials. *Angew. Chemie - Int. Ed.* **2010**, *49*, 6058–6082.
- (7) Kunkel, C.; Viñes, F.; Illas, F. Transition Metal Carbides as Novel Materials for CO<sub>2</sub> Capture, Storage, and Activation. *Energy Environ. Sci.* **2016**, *9*, 141–144.
- (8) Prats, H.; Stamatakis, M. Stability and Reactivity of Metal Nanoclusters Supported on Transition Metal Carbides. *Nanoscale Adv.* **2023**, *5*, 3214–3224.
- (9) Takahashi, T.; Sutherland, S.; Kozyr, A. *Global Ocean Surface Water Partial Pressure of CO<sub>2</sub> Database: Measurements Performed During 1957–2014 (Version 2014)*; Environmental Sciences Division: Oak Ridge National Laboratory, 2015.
- (10) Kunkel, C.; Viñes, F.; Ramírez, P. J.; Rodríguez, J. A.; Illas, F. Combining Theory and Experiment for Multitechnique Characterization of Activated CO<sub>2</sub> on Transition Metal Carbide (001) Surfaces. *J. Phys. Chem. C* **2019**, *123*, 7567–7576.
- (11) Morales-García, A.; Fernández-Fernández, A.; Viñes, F.; Illas, F. CO<sub>2</sub> Abatement Using Two-Dimensional MXene Carbides. *J. Mater. Chem. A* **2018**, *6*, 3381–3385.
- (12) Prats, H.; McAloone, H.; Viñes, F.; Illas, F. Ultra-Highly Selective Biogas Upgrading through Porous MXenes. *J. Mater. Chem. A* **2020**, *8*, 12296–12300.
- (13) Persson, L.; Halim, J.; Lind, H.; Hansen, T. W.; Wagner, J. B.; Näslund, L.-Å.; Darakchieva, V.; Palisaitis, J.; Rosen, J.; Persson, P. O. Å. 2D Transition Metal Carbides (MXenes) for Carbon Capture. *Adv. Mater.* **2018**, No. 1805472.
- (14) Kunkel, C.; Viñes, F.; Illas, F. Surface Activity of Early Transition-Metal Oxycarbides: CO<sub>2</sub> Adsorption Case Study. *J. Phys. Chem. C* **2019**, *123*, 3664–3671.
- (15) Pajares, A.; Prats, H.; Romero, A.; Viñes, F.; de la Piscina, P. R.; Sayós, R.; Homs, N.; Illas, F. Critical Effect of Carbon Vacancies on the Reverse Water Gas Shift Reaction over Vanadium Carbide Catalysts. *Appl. Catal. B* **2020**, *267*, No. 118719.
- (16) Kresse, G.; Furthmüller, J. Efficient Iterative Schemes for Ab Initio Total-Energy Calculations Using a Plane-Wave Basis Set. *Phys. Rev. B* **1996**, *54*, 11169–11186.
- (17) Perdew, J. P.; Burke, K.; Ernzerhof, M. Generalized Gradient Approximation Made Simple. *Phys. Rev. Lett.* **1996**, *77*, 3865–3868.
- (18) Grimme, S.; Antony, J.; Ehrlich, S.; Krieg, H. A Consistent and Accurate Ab Initio Parametrization of Density Functional Dispersion Correction (DFT-D) for the 94 Elements H-Pu. *J. Chem. Phys.* **2010**, *132*, No. 154104.
- (19) Blöchl, P. E. Projector Augmented-Wave Method. *Phys. Rev. B* **1994**, *50*, 17953–17979.
- (20) Kresse, G.; Joubert, D. From Ultrasoft Pseudopotentials to the Projector Augmented-Wave Method. *Phys. Rev. B* **1999**, *59*, 1758–1775.
- (21) Viñes, F.; Iglesias-Juez, A.; Illas, F.; Fernández-García, M. Hydroxyl Identification on ZnO by Infrared Spectroscopies: Theory and Experiments. *J. Phys. Chem. C* **2014**, *118*, 1492–1505.
- (22) Vázquez-Parga, D.; Jurado, A.; Roldán, A.; Viñes, F. A Computational Map of the Probe CO Molecule Adsorption and Dissociation on Transition Metal Low Miller Indices Surfaces. *Appl. Surf. Sci.* **2023**, *618*, No. 156581.
- (23) Garrido Torres, J. A.; Hansen, M. H.; Jennings, P. C.; Boes, J. R.; Bligaard, T. Low-Scaling Algorithm for Nudged Elastic Band Calculations Using a Surrogate Machine Learning Model. *Phys. Rev. Lett.* **2019**, *122*, No. 156001.
- (24) Ong, S. P.; Richards, W. D.; Jain, A.; Hautier, G.; Kocher, M.; Cholia, S.; Gunter, D.; Chevrier, V.; Persson, K. A.; Ceder, G. Python Materials Genomics (pymatgen): A Robust, Open-Source Python Library for Materials Analysis. *Comput. Mater. Sci.* **2013**, *68*, 314–319.
- (25) Larsen, A. H.; Mortensen, J. J.; Blomqvist, J.; Castelli, I. E.; Christensen, R.; Dulak, M.; Friis, J.; Groves, M. N.; Hammer, B.; Hargus, C.; Hermes, E. D.; Jennings, P. C.; Jensen, P. B.; Kermode, J.; Kitchin, J. R.; Kolsbjerg, E. L.; Kubal, J.; Kaasbjerg, K.; Lysgaard, S.; Maronsson, J. B.; Maxson, T.; Olsen, T.; Pastewka, L.; Peterson, A.; Rostgaard, C.; Schiøtz, J.; Schütt, O.; Strange, M.; Thygesen, K. S.; Vegge, T.; Vilhelmsen, L.; Walter, M.; Zeng, Z.; Jacobsen, K. W. The Atomic Simulation Environment—A Python Library for Working with Atoms. *J. Phys.: Condens. Matter* **2017**, *29*, No. 273002.
- (26) Stamatakis, M.; Vlachos, D. G. A Graph-Theoretical Kinetic Monte Carlo Framework for On-Lattice Chemical Kinetics. *J. Chem. Phys.* **2011**, *134*, No. 214115.
- (27) Stamatakis, M.; Vlachos, D. G. Unraveling the Complexity of Catalytic Reactions via Kinetic Monte Carlo Simulation: Current Status and Frontiers. *ACS Catal.* **2012**, *2*, 2648–2663.
- (28) Nielsen, J.; d'Avezac, M.; Hetherington, J.; Stamatakis, M. Parallel Kinetic Monte Carlo Simulation Framework Incorporating Accurate Models of Adsorbate Lateral Interactions. *J. Chem. Phys.* **2013**, *139*, No. 224706.
- (29) Prats, H. *ZacrosTools 2024*, GitHub repository, <https://github.com/hprats/ZacrosTools>.
- (30) Chong, X.; Jiang, Y.; Zhou, R.; Feng, J. The Effects of Ordered Carbon Vacancies on Stability and Thermo-Mechanical Properties of V<sub>8</sub>C<sub>7</sub> compared with VC. *Sci. Rep.* **2016**, *6*, 34007.
- (31) Lipatnikov, V. N.; Gusev, A. I.; Etmayer, P.; Lengauer, W. Phase Transformations in Non-Stoichiometric Vanadium Carbide. *J. Phys. Condens. Matter.* **1999**, *11*, 163–184.
- (32) Zhang, Y. F.; Viñes, F.; Xu, Y. J.; Li, J. Q.; Illas, F. Role of Kinetics in the Selective Surface Oxidations of Transition Metal Carbides. *J. Phys. Chem. B* **2006**, *110*, 15454–15458.
- (33) Viñes, F.; Sousa, C.; Illas, F.; Liu, P.; Rodríguez, J. A. A Systematic Density Functional Study of Molecular Oxygen Adsorption and Dissociation on the (001) Surface of Group IV-VI Transition Metal Carbides. *J. Phys. Chem. C* **2007**, *111*, 16982–16989.

- (34) Liu, G.; Zhao, Z. J.; Wu, T.; Zeng, L.; Gong, J. Nature of the Active Sites of VO<sub>x</sub>/Al<sub>2</sub>O<sub>3</sub> Catalysts for Propane Dehydrogenation. *ACS Catal.* **2016**, *6*, 5207–5214.
- (35) Kreissl, H. T.; Li, M. M. J.; Peng, Y. K.; Nakagawa, K.; Hooper, T. J. N.; Hanna, J. V.; Shepherd, A.; Wu, T. S.; Soo, Y. L.; Tsang, S. C. E. Structural Studies of Bulk to Nanosize Niobium Oxide with Correlation to their Acidity. *J. Am. Chem. Soc.* **2017**, *139*, 12670–12680.
- (36) Joseph, C.; Bourson, P.; Fontana, M. D. Amorphous to Crystalline Transformation in Ta<sub>2</sub>O<sub>5</sub> Studied by Raman Spectroscopy. *J. Raman Spectrosc.* **2012**, *43*, 1146–1150.
- (37) Arena, F.; Frusteri, F.; Parmaliana, A. Structure and Dispersion of Supported-Vanadia Catalysts. *Influence of the Oxide Carrier. Appl. Catal. A-Gen.* **1999**, *176*, 189–199.
- (38) Liu, X.; Kunkel, C.; Ramírez de la Piscina, P.; Homs, N.; Viñes, F.; Illas, F. Effective and Highly Selective CO Generation from CO<sub>2</sub> Using a Polycrystalline  $\alpha$ -Mo<sub>2</sub>C Catalyst. *ACS Catal.* **2017**, *7*, 4323–4335.
- (39) Wachs, I. E.; Chen, Y.; Jehng, J. M.; Briand, L. E.; Tanaka, T. Molecular Structure and Reactivity of the Group V Metal Oxides. *Catal. Today* **2003**, *78*, 13–24.
- (40) Prats, H.; Stamatakis, M. Breaking Linear Scaling Relationships with Transition Metal Carbides. *Catal. Sci. Technol.* **2023**, *13*, 4635–4639.
- (41) Preiss, H.; Schultze, D.; Klobes, P. Formation of NbC and TaC from Gel-Derived Precursors. *J. Eur. Ceram.* **1997**, *17*, 1423–1435.
- (42) Messner, M.; Walczyk, D. J.; Palazzo, B. G.; Norris, Z. A.; Taylor, G.; Carroll, J.; Pham, T. X.; Hettinger, J. D.; Yu, L. Electrochemical Oxidation of Metal Carbides in Aqueous Solutions. *J. Electrochem. Soc.* **2018**, *165*, H3107–H3114.
- (43) Prats, H.; Piñero, J. J.; Viñes, F.; Bromley, S. T.; Sayós, R.; Illas, F. Assessing the Usefulness of Transition Metal Carbides for Hydrogenation Reactions. *Chem. Commun.* **2019**, *55*, 12797–12800.
- (44) Prats, H.; Stamatakis, M. Atomistic and Electronic Structure of Metal Clusters Supported on Transition Metal Carbides: Implications for Catalysis. *J. Mater. Chem. A* **2022**, *10*, 1522–1534.